Nanoscale mapping by electron energy-loss spectroscopy reveals evolution of organic solar cell contact selectivity

CrossMark

Antonio Guerrero [a,*], Martin Pfannmöller [b], Alexander Kovalenko [a,1], Teresa S. Ripolles [a], Hamed Heidari [b], Sara Bals [b], Louis-Dominique Kaufmann [c], Juan Bisquert [a,d], Germà Garcia-Belmonte [a,*]

[a] Photovoltaic and Optoelectronic Devices Group, Departament de Física, Universitat Jaume I, ES-12071 Castelló, Spain
[b] EMAT, University of Antwerp, Antwerp, Belgium
[c] Genes'Ink, 24 Avenue Gaston Imbert, 13790 Rousset, France
[d] Department of Chemistry, Faculty of Science, King Abdulaziz University, Jeddah 21589, Saudi Arabia

ARTICLE INFO

ABSTRACT

Organic photovoltaic (OPV) devices are on the verge of commercialization being long-term stability a key challenge. Morphology evolution during lifetime has been suggested to be one of the main pathways accounting for performance degradation. There is however a lack of certainty on how specifically the morphology evolution relates to individual electrical parameters on operating devices. In this work a case study is created based on a thermodynamically unstable organic active layer which is monitored over a period of one year under non-accelerated degradation conditions. The morphology evolution is revealed by compositional analysis of ultrathin cross-sections using nanoscale imaging in scanning transmission electron microscopy (STEM) coupled with electron energy-loss spectroscopy (EELS). Additionally, devices are electrically monitored in real-time using the non-destructive electrical techniques capacitance–voltage (C–V) and Impedance Spectroscopy (IS). By comparison of imaging and electrical techniques the relationship between nanoscale morphology and individual electrical parameters of device operation can be conclusively discerned. It is ultimately observed how the change in the cathode contact properties occurring after the migration of fullerene molecules explains the improvement in the overall device performance.

© 2014 Elsevier B.V. All rights reserved.

1. Introduction

Organic photovoltaics (OPVs) devices have witnessed an impressive improvement in power conversion efficiencies (PCE) now reaching 10% for single layer bulk heterojunction (BHJ) solar cells [1]. However, device stability remains one of the key challenges for their commercialization. There are many factors affecting the device stability with moisture, heat and light regarded as the main stress factors [2]. Solution-processed OPVs are usually based on BHJ films of semiconducting polymers blended with a soluble fullerene derivative that form an interpenetrated bicontinuous network [3]. The organic layer harvests sun light and generates charges via charge transfer from the polymer (donor) to the fullerene (acceptor) that are collected at selective electrodes [3]. Performance of OPVs is strongly dependent on the donor/acceptor morphology [4] and variations of the

---

internal arrangement of donor and acceptor molecules is considered to be the main source of efficiency decrease limiting their potential commercialization [5].

Numerous studies have focused on the importance of the bulk morphology properties of the organic layer [6,7]. The use of additives [8], solvent annealing [9] and thermal treatments [10] can enhance the crystallinity and would increase the device efficiency. Enhanced crystallinity of the polymer phase have been correlated with high mobility [11] and improved device performance [12]. Importantly, intimately mixed donor/acceptor domains are required to provide optimum surface area to enable efficient charge separation [13]. However, the ability of PCBM molecules to diffuse through the blend film is often regarded as the primary cause of thermally induced degradation of solar cell performance [14]. The link between morphology modification and performance has usually been discussed in terms of the bulk properties of the active layer [15], but very little attention has been paid to the evolving properties of the active layer/outer contact interfaces. For example, molecular orientation of the polymer in intimate contact with the extracting electrode could be limiting the collection ability [16]. Indeed, morphology of the active layer in BHJ solar cells is frequently the result of a meta-stable configuration and several vertical segregation profiles can be formed [17]. Thermodynamically stable morphology blends can be obtained by using high transition temperature (T_g) polymers [18] or by cross-linking the organic phase [19]. In general terms one of the issues that still require intensive work is the understanding of specific mechanisms behind active layer/outer contact interface chemical and morphological evolution and its relationship to device performance.

Several morphology characterization techniques are currently available for organic photovoltaic devices and the reader is referred to two recent reviews [20,21]. For example, advanced techniques such as Grazing Incidence X-ray Diffraction (GXID) [22] or Electron Microscopy [13,23] provide access to the structure and length scales of the donor:acceptor domains. Alternatively, depth profile concentration of donor:acceptor blends can be analyzed by using Dynamic Secondary Ion Mass Spectroscopy (SIMS) [24], Variable-Angle Spectroscopic Ellipsometry (VASE) [17], Near-Edge X-ray Absorption Fine Structure Spectroscopy (NEXAFS) [25], etc. On the other hand, advanced electrical techniques are also available which allow understanding individual electrical processes taking place in an operating device. Techniques include Transient Absorption Spectroscopy (TAS) [26], Transient Photovoltage (TPV) [26], Capacitance–Voltage ($C–V$) [27] or Impedance Spectroscopy (IS) [28]. Interestingly electrical characterization offers the possibility to measure devices using non-destructive methods that enable real-time monitoring.

In this work a case study is created based on a thermodynamically unstable organic layer. The morphology evolution is correlated with the individual electrical processes taking place in the device, and revealed by compositional analysis of ultrathin cross-sections using spatially resolved electron energy-loss spectroscopy (EELS) in the analytical scanning transmission electron microscope (STEM). Additionally, devices are electrically monitored in real-time using the non-destructive electrical techniques $C–V$ and IS. By comparison of imaging and electrical techniques the relationship between morphology and photovoltaic parameter evolution in operating devices is conclusively established. It is ultimately observed how the change in the cathode contact properties occurring after the fullerene molecules migration explains the improvement in the overall device performance. The formation of a PCBM-rich layer contacting the ZnO electron-selective layer at the cathode causes both the increase in electron selectivity and establishes a good electrical connection between ZnO and the inner active layer fullerene molecules.

2. Results

2.1. Materials and solar cells fabrication

The method to produce the solar cells is based on standard processing conditions used in the literature [29,30]; full details can be found as Supporting Information and a brief description is provided here. Devices were prepared in the inverted configuration ITO/ZnO/P3HT:PCBM/MoO$_3$/Ag. Pre-cleaned patterned ITO was coated with commercially available ZnO nanoparticles to provide film thickness of about 50 nm. Substrates were heated at 100 °C for 5 min followed by a further treatment in the glovebox at 130 °C for 10 min. Spin coated P3HT:PCBM films (∼100 nm) were thermally treated at 130 °C for 10 min. Device fabrication was completed by thermal evaporation of MoO$_3$ (10 nm) and Ag (100 nm). Ten independent devices (4 pixels each) were encapsulated with epoxy and a glass slide for electrical characterization. Devices were kept in the glovebox in the dark at all times excluding the time required for electrical characterization (<15 min). Some un-encapsulated devices were kept in the glovebox for the whole period of the test to characterize the final state of the device using STEM measurements.

2.2. Film and device characterization

Cross-sections of devices were prepared by focused-ion-beam milling using a Helios NanoLab DualBeam (FEI) to a thickness of ∼45 nm [31]. For morphological studies of the cells cast from CHCl$_3$ and to prevent degradation or morphological changes due to storage of the ultrathin cross-sections, STEM investigations were conducted on the same day of FIB preparation. These were done with a Titan QU-Ant-EM microscope (FEI), operated at 120 kV and equipped with a GIF Quantum energy filter (Gatan). STEM dark-field imaging was used for visualization of the integrity of organic and inorganic layers. The pixel size for these images is 0.8 nm, which is sufficient to show the structure the ZnO layer. Afterwards hyperspectral STEM–SI data sets were acquired across all functional layers at a spatial resolution of 1.3 nm. Electron energy-loss spectra contain contributions from elastic and inelastic scattering up to 90 eV energy-loss, using a dispersion of 0.05 eV/pixel. The applied electron dose for dark-field and hyperspectral images was in total ∼300 e/A^2, which was shown to damage the electronic structure of the functional, organic materials but not the bulk plasmon

peak differences between P3HT and PCBM [32]. Data sets were processed and analyzed using Matlab (MathWorks). For this, hyperspectra were normalized to peak intensities and deconvolved to obtain the single-scattering contributions using a script made available by Egerton [31], followed by fitting a Gaussian to the plasmon peak. Center positions were mapped out to visualize the morphology of the organic layer. Film thickness was determined either by a VEECO DEKTACK 6M Stylus Profiler or—in case of the cross-sectional thickness—estimated using the energy loss signal [31]. Current density–voltage characteristics were carried out under illumination with a 1.5G source ($1000\,W\,m^{-2}$) using an Abet Sun 2000 Solar Simulator. The light intensity was adjusted with a calibrated Si solar cell. Capacitance–voltage and Impedance Spectroscopy measurements were performed using an Autolab PGSTAT-30 equipped with a frequency analyzer module. Capacitance was recorded at a frequency of 1000 Hz in the dark at several bias voltages to extract the capacitance–voltage characteristics. Impedance Spectroscopy was carried out under illumination conditions (1 sun) using a wide frequency range (100 Hz–1 MHz) at several applied DC voltages by applying a small voltage perturbation (20 mV rms).

2.3. Shelf-life efficiency

In order to generate a system to study the electrical implications of morphology evolution a polymer with a moderate transition temperature ($T_g \sim 120\,°C$) [33] as P3HT has been used in combination with a low boiling point solvent ($CHCl_3$), followed by thermal treatment. Using these conditions moderate crystalline polymer phases (see Supporting Information for XRD diffraction pattern) are obtained implying that thermodynamically stable morphologies will not be attained. An inverted configuration composed of $ITO/ZnO/P3HT:PCBM/MoO_3/Ag$ is chosen to minimize any degradation arising from the contacts. Devices are characterized by their current density–voltage (*J*–*V*) curves measured over a period of one year using non-accelerated conditions (absence of oxygen, water or light). By using this methodology any change in performance will be due exclusively to a morphology evolution of the active layer blend. As expected for devices processed from chloroform adequate morphology of donor an acceptor is not achieved and initial efficiencies are below 1% [34]. The morphology evolution occurring during a period of one year led to a two-fold increase in efficiency. Initial and final photovoltaic parameters are summarized in Table 1.

Fig. 1 shows that this system provides a good example of morphology evolving devices. Individual photovoltaic parameters change following two different time trends.

Whilst the open circuit voltage (V_{oc}) increases dramatically during the first 10–20 h the short circuit current (J_{sc}) increases gradually more than 30% over the whole period of study. Alternatively, fill factor (FF) is always stable and low. Overall, the V_{oc} increases by 74 mV (~10%) and J_{sc} increases nearly by 3 mA/cm² (45%). As device performance parameters are the outcome of many different optical and electrical processes, *J*–*V* curves cannot help identifying specific mechanisms behind the reported evolution. To obtain deeper knowledge the use of more advanced electrical techniques is needed.
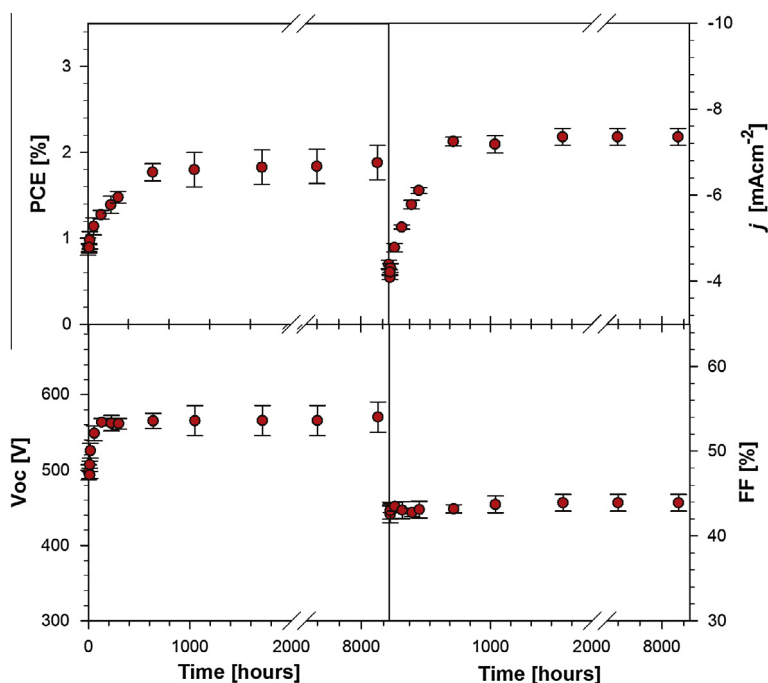
2.4. Morphology and vertical phase segregation analyzed by electron energy-loss nanoscale mapping

Pristine and aged devices cast from $CHCl_3$ followed by a thermal treatment at 130 °C have been analyzed using advanced microscopy techniques. We apply STEM in combination with EELS to visualize the morphology of photoactive layers in cross-sectional samples prepared using focused ion beam. This combination is called STEM spectral imaging (STEMSI) and offers spatially resolved low energy-loss spectroscopy at the nanoscale. After fitting a Gaussian profile to each spectrum, the determined mean positions can be mapped out. Resulting maps indicate plasmon peak positions, which differ depending on the localized enrichment of a certain material or on the amount of intermixing. Fig. 2a and b shows STEMSI maps of bulk plasmon peak positions, which can typically be found between 20 and 25 eV for carbon based materials [31]. However, for polymers and fullerenes both center and shape of plasmons differ [13]. Hence, by acquiring energy loss spectra comprising such low energies, it is possible to obtain reliable, qualitative maps of the morphology at nanometer resolution, applying a relatively small electron dose. These device states correspond to the performance parameters summarized in Table 1. As evidenced by such morphological analysis of focused ion beam cross-sections of both fresh and aged samples, fullerene content at the ZnO-covered cathode increases dramatically during the course of the experiment (red color in Fig. 2a and b). Evolution of morphology in aged samples shows a qualitatively small increase of demixing accompanied by a slight decrease of the intermixed phase, but a highly PCBM-rich layer develops contacting the upper ZnO layer. This observation entails an overall morphological change which produces as a result a vertical segregation of fullerene molecules accumulated at the cathode contact. To verify whether the PCBM accumulation at the cathode contact causes the observed increment in the photovoltaic parameters purely electrical techniques are further used to monitor how fullerene cathode content evolves over time.

Table 1
Photovoltaic parameters for fresh and aged devices processed under different conditions. Electrical parameters extracted from *J*–*V* curves, and capacitance–voltage are included.

Device	J_{sc} (mA cm^{-2})	V_{oc} (mV)	FF (%)	PCE (%)	N ($\times 10^{16}$ cm^{-3})	V_{FB} (mV)	Fullerene cathode content (%)	Leakage Current (dark – 1 V) (mA cm^{-2})
Fresh	4.4	496	41	0.90	4.0	610	70	2.4
Aged	7.3	570	43	1.90	10.0	409	100	0.3

Fig. 1. Device performance parameters extracted from J–V curves measured during a period of 1 year for devices fabricated with the architecture ITO/ZnO/P3HT:PCBM/MoO$_3$/Ag and active layer cast from chloroform (CHCl$_3$).
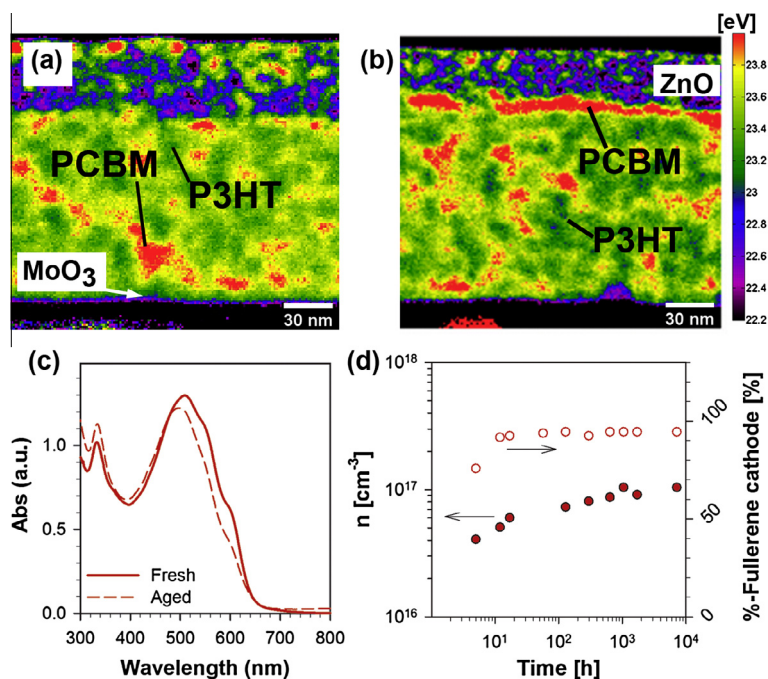
Fig. 2. Maps showing plasmon peak positions of ultrathin cross-sections of devices cast from chloroform (a) fresh and (b) aged. Red color denotes PCBM enriched phases (higher plasmon energy) and green color P3HT enriched phases (lower plasmon energy). The maps are created from spatially resolved low energy loss STEMSI data at a resolution of 1.3 nm. Evolution of morphology in aged samples shows that demixing and distribution of domains does not change but that a highly PCBM-rich layer develops at the ZnO-covered contact. (c) Absorption spectra of fresh and aged films cast from CHCl$_3$. (d) Evolution of defect density values (n) with shelf storage and calculated fullerene content at the cathode interface extracted from capacitance–voltage measurements carried out in the dark of devices cast from CHCl$_3$. (For interpretation of the references to color in this figure legend, the reader is referred to the web version of this article.)

2.5. Correlation with electrical measurements

We have recently shown how to extract relevant information about the fullerene content contacting the device cathode by means of capacitance–voltage (*C–V*) analysis [27,30]. This technique allows determining the fullerene content at the cathode which is directly related to the contact selectivity. *C–V* is non-destructive and can be used in complete devices in real time experiments. A small AC voltage perturbation is applied to a working device at varying DC voltage biases and the differential current output is measured. For OPVs *C–V* is typically carried out at a certain frequency between 100 and 1000 Hz (see Supporting Information for details), and offers information on the energy level equilibration at the organic layer/cathode interface where a dipole layer is generated by chemical reduction of the fullerene molecules present at that interface [27]. Additionally, a confined electrical field at the vicinity of the cathode appears producing band bending (depletion zone) in the adjacent active layer.

The fullerene content at the cathode interface is calculated by analysis of the *C–V* data [30] as a function of the degradation time, and representative values are shown in Fig. 1d. Initially, the fullerene content at the cathode is relatively low (~70%) and during the first tens of hours this value increases to nearly full coverage. In addition to the increase in contact selectivity, there is a correlation between fullerene molecules covering the cathode and the leakage current measured under dark conditions (see Table 1 and Fig. SI3) [30]. In this case the leakage current decreases over one order of magnitude during the first 20 h. The timescale of this modification correlates with the increase in V_{oc} as observed in Fig. 1.

Along with fullerene content at the cathode, defect density (polymer *p*-doping level) can be extracted from *C–V* measurements by analyzing Mott–Schottky plots (see Supporting Information for details). It is known that defect density is connected with the crystallinity of the P3HT domains [35] and with chemical modification due to external dopants [36]. As devices are not exposed in these experiments to external agents, defect density will be due exclusively to modification in the crystallinity of the P3HT domains. Initial defect levels (Table 1) are higher than those typically observed for relatively high crystalline films cast from ODCB (~5 × 10^{15} cm^{-3}) [35]. This result is in agreement with the low crystallinity of the active layer observed in the XRD diffraction patterns, and absorption measurements (shown as Supporting Information). The defect density increases as a function of time in agreement with the observed reduction in crystallinity as evidenced by the film absorption measurements (Fig. 2c). Importantly, the increase in defect density occurs gradually during the whole year (Fig. 2d) which is related to the FF as it will be discussed below.

In order to better understand the electrical losses the resistive response of devices are studied by IS under illumination conditions. This technique provides access to series resistance [37], recombination kinetics [38] and transport properties [39]. The working principle of *C–V* and IS is similar, however, in the latter the AC voltage frequency is varied over a wide range (1 Hz–1 MHz). Representative

spectra are shown as Supporting Information together with the equivalents circuits used to fit the impedance data displayed in Fig. 3. The meaning of each of the parameters that can be extracted from fitting will be briefly described here. All Nyquist plots show two arcs at high applied voltages, and a contribution at still lower frequencies is observed only for the fresh sample, previously connected to a contact resistance (R_{CO}) [40]. Values of 30–75 Ω cm^2 are observed for R_{CO} being this a significant contribution to the overall series resistance of the device. Interestingly, this resistance is not present in aged devices indicating that in the initial state the fullerene is only partially able to transfer electrons to the ZnO increasing as a consequence the contact resistance. In the final state the active layer/ZnO interface is enriched with fullerenes and the charge transfer is facilitated reducing the values of R_{CO} which is no longer observed. As it will be explained below the presence of this R_{CO} limits the photocurrent extracted in the fresh device.

The impedance features in the high frequency region have previously been correlated with resistive processes caused by carrier movement (R_{tr}), also contributing to the series resistance of the device [37]. This is normally observed in non optimized devices when morphology issues limit efficient transport of carriers [28,39]. For fresh devices R_{tr} is relatively small 2–15 Ω cm^2 indicating that the low FF observed is the consequence of the high R_{CO}. On the other hand, aged devices show values of about 20–100 Ω cm^2. This notable increase in R_{tr} is correlated with the increase in defect density that impedes the efficient transport of carriers. The low frequency impedance response corresponds to the recombination resistance (R_{rec}) present in all photovoltaic devices, which represents the opposition of the system to free carrier recombination [38]. High R_{rec} are desired as this is a sign of low recombination fluxes [41]. At low applied voltages the extracted R_{rec} shows similar values for fresh and aged devices indicating that the reduction of R_{CO} for the aged device is totally compensated by the increase in R_{tr}. However, for the fresh device and above 0.25 V the system is not able to increase the photogenerated carrier density (related to
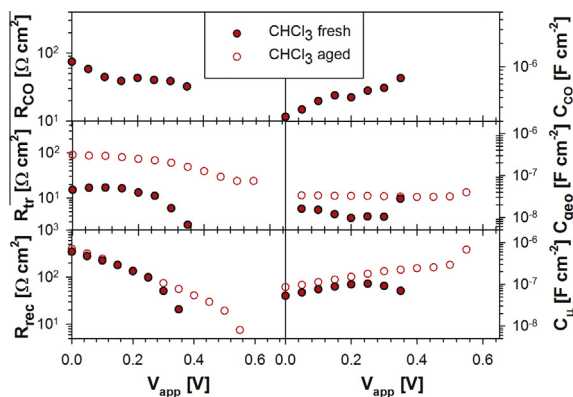

Fig. 3. Fitting results extracted from Impedance Spectroscopy data for representative devices measured in the initial state (fresh) and at the end of the lifetime (aged). The equivalent circuits used are shown as supporting information.

the values attained by the chemical capacitance C_μ) and recombination takes place more readily.

3. Discussion

As discussed previously, shelf life evolution of photovoltaic parameters in Fig. 1 exhibit three different trends. V_{oc} shows a subtle increment within the first 100 h and then remains stable. J_{sc} evolves much more slowly and reaches its maximum after 600 h. On the contrary FF remains rather constant throughout the experiment. Long term stability does not change any more as observed in Fig. 1a. It is known that the origin of the V_{oc} is related to energetic [42] and kinetic mechanisms [43]. Indeed, the difference between the donor HOMO and the acceptor LUMO determines V_{oc} as a first approximation [44]. In addition, gap defect states are known to modulate the Fermi level position that ultimately establishes the output V_{oc} [35]. Increased defect density in the aged device should in theory decrease the V_{oc} as these defects reduce Fermi level shift upon illumination. However, in this work V_{oc} increases and results from STEM, capacitance–voltage and Impedance Spectroscopy provide a clear answer on the nature of such an improvement. This increase follows the same time scale as the increase in the contact selectivity indicating that originally the device was seriously limited by an inefficient connection between the cathode and the active layer fullerene molecules. Moreover this poor electrical connection is evidenced by the large contact resistance extracted from IS of fresh devices. After morphology evolution caused by the presence of meta-stable phases, the cathode contact gains fullerene molecules, becoming more electron selective. Consequently the resistance associated to the contact electron hindrance disappears allowing for the V_{oc} increase. The presence of a sufficiently high fullerene covering of the cathode interface as a necessary condition for efficient device operation was demonstrated in previous work [30].

Balance among different resistive mechanisms lies behind the stable trend exhibited by FF. Three different contributions are expected to influence FF: (i) a reduction in the overall series resistance mainly caused by decrease in R_{CO}, (ii) increase in transport resistance and (iii) the observation of similar recombination kinetics. The overall series resistance of OPV devices is dominated by the resistance associated to the contacts [45]. Here very high contact resistances are found for fresh devices of up to 75 Ω cm^2 at 0 V (Fig. 3) that is clearly limiting the extracted charge. Then the series resistance decreases during the lifetime as R_{CO} is not present for aged devices. On the other hand, R_{tr} is also a source of resistive losses and in all cases this resistive contribution is observed for devices casted from CHCl$_3$ [46]. However, the magnitude of this parameter is relatively low for fresh devices (<20 Ω cm^{-2}) and increases with the presence of more electrically active defects (20–85 Ω cm^{-2}). It is noted that the increment in R_{tr} roughly compensates the enhanced cathode connection (R_{CO} disappearance). Finally, values of R_{rec} as a function of the applied bias are very similar. Overall, the improvement in the series resistance appears to be

dominant over the increase in the resistance related to transport as the FF slightly increases during the test.

Increment in J_{sc} during the first 600 h should be related to a combination of several factors. The maximum current calculated by integration of the absorption spectra provides values of 12 mA cm^{-2}. This is the current that could be obtained if no electrical losses would be taking place. However, only 4–7 mA cm^{-2} are extracted at short circuit. Therefore, almost half of photons are lost due to inefficient physical processes occurring during device operation. As no significant difference in absorption degree between fresh and aged films occurs (see Fig. 2c) the increase in J_{sc} must arise from the partial suppression of inner loss mechanisms. In devices limited by high series resistance J_{sc} may be seriously affected [46]. An important decrease in R_{CO} takes place during the lifetime, being no longer observed after the device test, and this enables a more efficient extraction of carriers to the electrodes and improves collecting efficiency. However, contact selectivity increment (inferred from the fullerene covering in Fig. 2d) occurs subtly after device construction (<100 h). Alternatively, the transport resistance R_{tr} is observed to increase during the experiment which is in good agreement with the augment of the defect density in Fig. 2d. An additional factor which contributes to the collected current is the increment in photogenerated carrier density. Using analytical transmission electron microscopy it was previously shown that the extracted photocurrent largely depends on the nanoscale morphology features [13]. Here, we observe a qualitatively small increase of demixing accompanied by a slight decrease of the intermixed phase (Fig. 2a and b). Importantly, this modification of the morphology in the bulk of the active layer is expected to take place gradually over the whole study, and might assist photogeneration.

4. Conclusion

In summary, a case study that provides morphology evolving organic layers is generated and initial and final states have been analyzed by advanced microscopy techniques. Compositional analysis of ultrathin cross-sections using spatially resolved electron energy-loss spectra in the analytical STEM reveals that active layer morphology evolves forming a PCBM-rich layer at the organic layer/ ZnO interface. Evolution in morphology yields a change in the vertical segregation profile that leads to an increase in the contact selectivity accompanied by a good electrical connection between the cathode and active layer fullerene molecules. Devices are further electrically characterized by using C–V and IS techniques to confirm the increase in fullerene covering at the cathode interface. We highlight how the change in cathode contact properties and improvement in overall device performance can be explained by fullerene molecules migration.

Appendix A. Supplementary data

Supplementary data associated with this article can be found, in the online version, at http://dx.doi.org/10.1016/j.orgel.2014.11.007.

References

[1] Z. He, C. Zhong, S. Su, M. Xu, H. Wu, Y. Cao, Nat. Photon. 6 (9) (2012) 591–595.
[2] M. Jørgensen, K. Norrman, S.A. Gevorgyan, T. Tromholt, B. Andreasen, F.C. Krebs, Adv. Mater. (Weinheim, Germany) 24 (5) (2012) 580–612.
[3] G. Yu, J. Gao, J.C. Hummelen, F. Wudl, A.J. Heeger, Science 270 (5243) (1995) 1789–1791.
[4] X. Yang, J. Loos, S.C. Veenstra, W.J.H. Verhees, M.M. Wienk, J.M. Kroon, M.A.J. Michels, R.A.J. Janssen, Nano Lett. 5 (4) (2005) 579–583.
[5] Z. Li, H.C. Wong, Z. Huang, H. Zhong, C.H. Tan, W.C. Tsoi, J.S. Kim, J.R. Durrant, J.T. Cabral, Nat. Commun. 4 (2013) 2227.
[6] S. Günes, H. Neugebauer, N.S. Sariciftci, Chem. Rev. (Washington, DC, United States) 107 (4) (2007) 1324–1338.
[7] M.A. Brady, G.M. Su, M.L. Chabinyc, Soft Matter 7 (2011) 11065.
[8] M.T. Dang, J.D. Wuest, Chem. Soc. Rev. 42 (23) (2013) 9105–9126.
[9] G. Li, V. Shrotriya, J. Huang, Y. Yao, T. Moriarty, K. Emery, Y. Yang, Nat. Mater. 4 (11) (2005) 864–868.
[10] W. Ma, C. Yang, X. Gong, K. Lee, A.J. Heeger, Adv. Funct. Mater. 15 (10) (2005) 1617–1622.
[11] H. Sirringhaus, N. Tessler, R.H. Friend, Science 280 (5370) (1998) 1741–1744.
[12] Y. Chen, X. Wan, G. Long, Acc. Chem. Res. 46 (11) (2013) 2645–2655.
[13] M. Pfannmöller, H. Flügge, G. Benner, I. Wacker, C. Sommer, M. Hanselmann, S. Schmale, H. Schmidt, F.A. Hamprecht, T. Rabe, W. Kowalsky, R.R. Schröder, Nano Lett. 11 (2011) 3099–3107.
[14] S. Ebadian, B. Gholamkhass, S. Shambayati, S. Holdcroft, P. Servati, Sol. Energy Mater. Sol. Cells 94 (12) (2010) 2258–2264.
[15] F.C. Jamieson, E.B. Domingo, T. McCarthy-Ward, M. Heeney, N. Stingelin, J.R. Durrant, Chem. Sci. 3 (2) (2012) 485–492.
[16] B.A. Collins, J.E. Cochran, H. Yan, E. Gann, C. Hub, R. Fink, C. Wang, T. Schuettfort, C.R. McNeill, M.L. Chabinyc, H. Ade, Nat. Mater. 11 (6) (2012) 536–543.
[17] M. Campoy-Quiles, T. Ferenczi, T. Agostinelli, P.G. Etchegoin, Y. Kim, T.D. Anthopoulos, P.N. Stavrinou, D.D.C. Bradley, J. Nelson, Nat. Mater. 7 (2) (2008) 158–164.
[18] I.T. Sachs-Quintana, T. Heumüller, W.R. Mateker, D.E. Orozco, R. Cheacharoen, S. Sweetnam, C.J. Brabec, M.D. McGehee, Adv. Funct. Mater. 24 (25) (2014) 3978–3985.
[19] Z. Li, H.C. Wong, Z. Huang, H. Zhong, C.H. Tan, W.C. Tsoi, J.S. Kim, J.R. Durrant, J.T. Cabral, Nat. Commun. (2013) 4.
[20] W. Chen, M.P. Nikiforov, S.B. Darling, Energy Environ. Sci. 5 (8) (2012) 8045–8074.
[21] M. Pfannmöller, W. Kowalsky, R.R. Schröder, Energy Environ. Sci. 6 (2013) 2871–2891.
[22] J. Rivnay, S.C.B. Mannsfeld, C.E. Miller, A. Salleo, M.F. Toney, Chem. Rev. (Washington, DC, United States) 112 (2012) 5488–5519.
[23] S.S.v. Bavel, E. Sourty, G.d. With, J. Loos, Nano Lett. 9 (2009) 507–513.
[24] C.M. Björström, S. Nilsson, A. Bernasik, A. Budkowski, M. Andersson, K.O. Magnusson, E. Moons, Appl. Surf. Sci. 253 (8) (2007) 3906–3912.
[25] S. Zhu, Y. Liu, M.H. Rafailovich, J. Sokolov, D. Gersappe, D.A. Winesett, H. Ade, Nature 400 (6739) (1999) 49–51.
[26] G. Grancini, D. Polli, D. Fazzi, J. Cabanillas-Gonzalez, G. Cerullo, G. Lanzani, J. Phys. Chem. Lett. 2 (9) (2011) 1099–1105.
[27] A. Guerrero, L.F. Marchesi, P.P. Boix, S. Ruiz-Raga, T. Ripolles-Sanchis, G. Garcia-Belmonte, J. Bisquert, ACS Nano 6 (4) (2012) 3453–3460.
[28] A. Guerrero, N.F. Montcada, J. Ajuria, I. Etxebarria, R. Pacios, G. Garcia-Belmonte, E. Palomares, J. Mater. Chem. A 1 (39) (2013) 12345–12354.
[29] J. Ajuria, I. Etxebarria, W. Cambarau, U. Munecas, R. Tena-Zaera, J.C. Jimeno, R. Pacios, Energy Environ. Sci. 4 (2) (2011) 453–458.
[30] A. Guerrero, B. Dörling, T. Ripolles-Sanchis, M. Aghamohammadi, E. Barrena, M. Campoy-Quiles, G. Garcia-Belmonte, ACS Nano 7 (5) (2013) 4637–4646.
[31] R.F. Egerton, Electron Energy-Loss Spectroscopy in the Electron Microscope, Springer, New York, 2011.
[32] M. Pfannmöller, H. Flügge, G. Benner, I. Wacker, W. Kowalsky, R.R. Schröder, Synth. Met. 161 (23–24) (2012) 2526–2533.
[33] C. Lungenschmied, S. Bauer, R. Schwödiauer, S. Rodman, D. Fournier, G. Dennler, C.J. Brabec, J. Appl. Phys. 109 (4) (2011). 044503-044503-5.
[34] S. Miller, G. Fanchini, Y.-Y. Lin, C. Li, C.-W. Chen, W.-F. Su, M. Chhowalla, J. Mater. Chem. 18 (3) (2008) 306–312.
[35] T.S. Ripolles, A. Guerrero, G. Garcia-Belmonte, Appl. Phys. Lett. 103 (24) (2013) 243306.
[36] A. Guerrero, P.P. Boix, L.F. Marchesi, T. Ripolles-Sanchis, E.C. Pereira, G. Garcia-Belmonte, Sol. Energy Mater. Sol. Cells 100 (2012) 185–191.
[37] A. Guerrero, T. Ripolles-Sanchis, P.P. Boix, G. Garcia-Belmonte, Org. Electron. 13 (11) (2012) 2326–2332.
[38] P.P. Boix, A. Guerrero, L.F. Marchesi, G. Garcia-Belmonte, J. Bisquert, Adv. Energy Mater. 1 (6) (2011) 1073–1078.
[39] A. Guerrero, S. Loser, G. Garcia-Belmonte, C.J. Bruns, J. Smith, H. Miyauchi, S.I. Stupp, J. Bisquert, T.J. Marks, Phys. Chem. Chem. Phys. 15 (39) (2013) 16456–16462.
[40] A. Guerrero, S. Chambon, L. Hirsch, G. Garcia-Belmonte, Adv. Funct. Mater. 24 (2014) 6234–6240.
[41] T. Ripolles-Sanchis, S.R. Raga, A. Guerrero, M. Welker, M. Turbiez, J. Bisquert, G. Garcia-Belmonte, J. Phys. Chem. C 117 (17) (2013) 8719–8726.
[42] C.J. Brabec, A. Cravino, D. Meissner, N.S. Sariciftci, T. Fromherz, M.T. Rispens, L. Sanchez, J.C. Hummelen, Adv. Funct. Mater. 11 (5) (2001) 374–380.
[43] J. Bisquert, G. Garcia-Belmonte, J. Phys. Chem. Lett. 2 (2011) 1950–1964.
[44] J. Widmer, M. Tietze, K. Leo, M. Riede, Adv. Funct. Mater. 23 (2013) 5814–5821.
[45] T. Ripolles-Sanchis, A. Guerrero, J. Bisquert, G. Garcia-Belmonte, J. Phys. Chem. C 116 (32) (2012) 16925–16933.
[46] R. Steim, F.R. Kogler, C.J. Brabec, J. Mater. Chem. 20 (13) (2010) 2499–2512.